



RESEARCH ARTICLE

10.1029/2023JA031690

Ionospheric Flow Vortex Induced by the Sudden Decrease in the Solar Wind Dynamic Pressure

Yaqi Jin¹ , Jøran Idar Moen^{1,2}, Andres Spicher³ , Jianjun Liu⁴ , Lasse B. N. Clausen¹ , and Wojciech J. Miloch¹ 

¹Department of Physics, University of Oslo, Oslo, Norway, ²University Centre in Svalbard, Longyearbyen, Norway,

³Department of Physics and Technology, UIT the Arctic University of Norway, Tromsø, Norway, ⁴SOA Key Laboratory for Polar Science, Polar Research Institute of China, Shanghai, China

Key Points:

- An ionospheric flow vortex was likely triggered by the sudden decrease in the solar wind dynamic pressure
- The flow vortex resulted in a reduction of the electron density
- In the morning sector, the flow vortex was clockwise and associated with upward field-aligned current and downward electron precipitation

Supporting Information:

Supporting Information may be found in the online version of this article.

Correspondence to:

Y. Jin,
yaqi.jin@fys.uio.no

Citation:

Jin, Y., Moen, J. I., Spicher, A., Liu, J., Clausen, L. B. N., & Miloch, W. J. (2023). Ionospheric flow vortex induced by the sudden decrease in the solar wind dynamic pressure. *Journal of Geophysical Research: Space Physics*, 128, e2023JA031690. <https://doi.org/10.1029/2023JA031690>

Received 10 MAY 2023

Accepted 13 OCT 2023

Abstract Abrupt changes in the solar wind dynamic pressure can greatly affect the Earth's magnetosphere-ionosphere system. We present an ionospheric flow vortex in the morning sector during the sudden decrease in the solar wind dynamic pressure. The flow vortex was clearly observed by both the Hankasalmi radar and the azimuthal scan mode of the European Incoherent Scatter (EISCAT) Svalbard Radar (ESR). The flow vortex was first seen in the eastern field of view (FOV) of the Hankasalmi radar, and then propagated poleward and westward into the FOV of the ESR. During the passage of the flow vortex, a gradual decrease of electron density was observed by the field-aligned ESR 42 m antenna. When the equatorward directed ionospheric flow reached the ESR site, weak and visible increases in the electron density and electron temperature were observed. This impact was likely caused by soft electron precipitation associated with the clockwise flow vortex and upward field-aligned current. The azimuthal scan mode of the ESR 32 m radar at low elevation angle (30°) allowed us to measure key ionospheric parameters over a larger area (6° in latitude and 120° in azimuthal angle). The latitudinal scan of the electron temperature was used to proxy the equatorward auroral boundary, which shows that the flow vortex was located in the subauroral region. We further demonstrated that it is possible to study the weak increase of electron density by using GPS total electron content (TEC) data. A minor TEC increase was observed near the center of the flow vortex.

1. Introduction

The Earth's magnetosphere-ionosphere system can be greatly affected by abrupt changes in the solar wind dynamic pressure. For example, the sudden increase in the solar wind dynamic pressure associated with a fast interplanetary shock can cause significant compression of the magnetosphere. Consequently, a positive geomagnetic sudden impulse (SI+) can be observed using ground-based magnetometers (e.g., Araki, 1994). Several phenomena can result from the compression of the magnetosphere. For example, the intensification of auroral luminosity can be found first near local noon, and then the intensification propagates to the nightside along the dawn and dusk flanks of the auroral oval (Meurant et al., 2003; Zhou & Tsurutani, 1999; Zhou et al., 2003). The sudden increase of the solar wind dynamic pressure can also induce traveling convection vortices (TCVs), which are east-west aligned pairs of oppositely directed flow vortices (Friis-Christensen et al., 1988). Once generated, the TCVs propagate tailward away from local noon in the high-latitude ionosphere with a speed of several km/s (Friis-Christensen et al., 1988; Glassmeier et al., 1989; Lühr et al., 1996). The ionospheric flow vortices associated with TCVs have been observed by incoherent scatter radars (Lühr et al., 1996; Valladares et al., 1999) and Super Dual Auroral Radar Network (SuperDARN) radars (Kataoka et al., 2003; Liu et al., 2011, 2015, 2023; Lyatsky et al., 1999).

Though there exist many studies on the ionospheric effect due to the sudden solar wind pressure increase in the literature (Collis & Haggstrom, 1991; Schunk et al., 1994; Zou et al., 2017), studies on the impact of negative solar wind pressure pulses and magnetosphere expansion are quite rare. Early studies focused on the magnetic field perturbations related to the dynamic pressure decrease (Araki & Nagano, 1988; Takeuchi et al., 2002a). More recently, by using the SuperDARN King Salmon radar, Hori et al. (2012) reported poleward propagating vortex-like flow structures in the evening sector (~19 magnetic local time (MLT)) which were induced by a negative sudden impulse of the solar wind pressure. In another study, Zhao et al. (2016) reported a magnetospheric flow vortex that was driven by a negative solar wind dynamic pressure pulse. It has been found that the direction of the flow vortex was opposite to the scenario due to positive solar wind

© 2023 The Authors.

This is an open access article under the terms of the [Creative Commons Attribution-NonCommercial License](https://creativecommons.org/licenses/by-nc/4.0/), which permits use, distribution and reproduction in any medium, provided the original work is properly cited and is not used for commercial purposes.

pressure pulses. By using the ground-based all-sky imager, the enhancement of the auroral luminosity has been found in the dawnside (~ 5 MLT) ionosphere in associated with an upward field-aligned current (FAC) (Zhao et al., 2019).

Besides the sudden changes in the solar wind dynamic pressure, another important mechanism that transfers momentum and energy to the magnetosphere-ionosphere system is magnetic reconnection (Dungey, 1961). The flux transfer event (FTE) is used to describe the transient, pulsed reconnection at the dayside magnetopause (Haerendel et al., 1978; Lockwood & Hapgood, 1998; Russell & Elphic, 1978, 1979). Southwood (1987) proposed a model to explain the ionospheric signatures of FTEs. In the Southwood model, a pair of field-aligned currents (FACs) with opposite direction is generated on the poleward and equatorward edge of the newly reconnected flux tube. The pair of FACs sets up a twin vortex flow pattern on both sides of the newly reconnected flux tube. Later, by using the fast azimuth sweeps of the EISCAT Svalbard radar (ESR), Rinne et al. (2007) found that the return flow of the newly reconnected flux never formed simultaneously in pairs. As a result, an asymmetric version of the Southwood FTE model was proposed, where the return flow only occurs on the poleward side of the newly reconnected flux tube and this was termed as reversed flow event (RFE) (Moen et al., 2008; Rinne et al., 2007).

In this study, we report an event of ionospheric flow vortex in the morning side ionosphere. As will be shown later, this event is likely driven by an abrupt, step function like decrease in the solar wind dynamic pressure. The used instruments and data sets are introduced in Section 2. Section 3 presents the event in detail, following by a summary and discussion in Section 4.

2. Instrumentation and Data Set

In this study, we use the European Incoherent Scatter (EISCAT) Svalbard Radar (ESR) in Longyearbyen, the SuperDARN radar in Hankasalmi, Finland, and Global Positioning System (GPS) receiver in Ny-Ålesund.

The ESR in Longyearbyen (78.15°N, 16.02°E; magnetic latitude (MLAT) 75.43°N) consists of a 32-m steerable antenna and a 42-m static field-aligned antenna (azimuth = 182.1°, elevation = 81.6°). The basic ionospheric properties such as the electron density (Ne), electron temperature (Te), ion temperature (Ti), and line-of-sight ion velocity (Vi) can be obtained from both antennas (e.g., Wannberg et al., 1997). On 3 December 2011, the ESR 32 m antenna was operated in a fast azimuth scan mode from 6:30 to 8:30 UT to study the RFEs (Carlson et al., 2002; Rinne et al., 2007). The 32-m antenna beam moved between azimuth angles of 180° and 300° at an elevation angle of 30° and was alternating between clockwise and anticlockwise motion. With the highest allowed azimuthal scan speed of 0.625°/s, the radar beam completes one 120° azimuthal scan in 192 s. The selected pulse code *taro* allows for simultaneous transmission and receiving of signals by both antennas. The stored data resolution is 6.4 s, which results in 30 adjacent radar beam directions in one complete azimuthal scan. For the data from the ESR 42 m antenna, the data are analyzed using GUISDAP with integration time of 64 s.

For the ionospheric drift velocities, we use the data from the coherent scatter high frequency (HF) radar in Hankasalmi (62.3°N, 26.6°E) from SuperDARN (Greenwald et al., 1995; Milan et al., 1999). The HF radar operates in 16 azimuthal beams that are separated by about 3.2°. By analyzing the backscatter echoes from field-aligned ionospheric irregularities, the line-of-sight Doppler drift velocity, spectral width, and power can be obtained. We use the SuperDARN data at the FITACF level, which is a commonly used routine to process SuperDARN auto-correlation functions (see e.g., Ribeiro et al., 2013).

The solar wind data from the OMNI database are used to present the upstream solar wind conditions (King & Papitashvili, 2005). The OMNI interplanetary magnetic field (IMF) is presented in the geocentric solar magnetospheric coordinates. The Sym-H index and AE indices in 1-min resolution is used to show the global magnetic response to the solar wind variations. The Sym-H and AE indices were obtained from the World Data Center for Geomagnetism at Kyoto University (<http://wdc.kugi.kyoto-u.ac.jp/>).

The GPS data in Ny-Ålesund (78.9°N, 11.9°E) is taken from the International Global Navigation Satellite System (GNSS) Service. The Receiver Independent Exchange Format (RINEX) format data in 1-s resolution is downloaded from the high-rate data of NASA's Crustal Dynamics Data Information System (CDDIS) <https://cddis.nasa.gov/archive/gnss/data/ighrate/>. The carrier phase observations at L1 and L2 bands are used to calculate the total electron content (TEC). In this study, we only use 1-s resolution TEC data from GPS satellite 31.

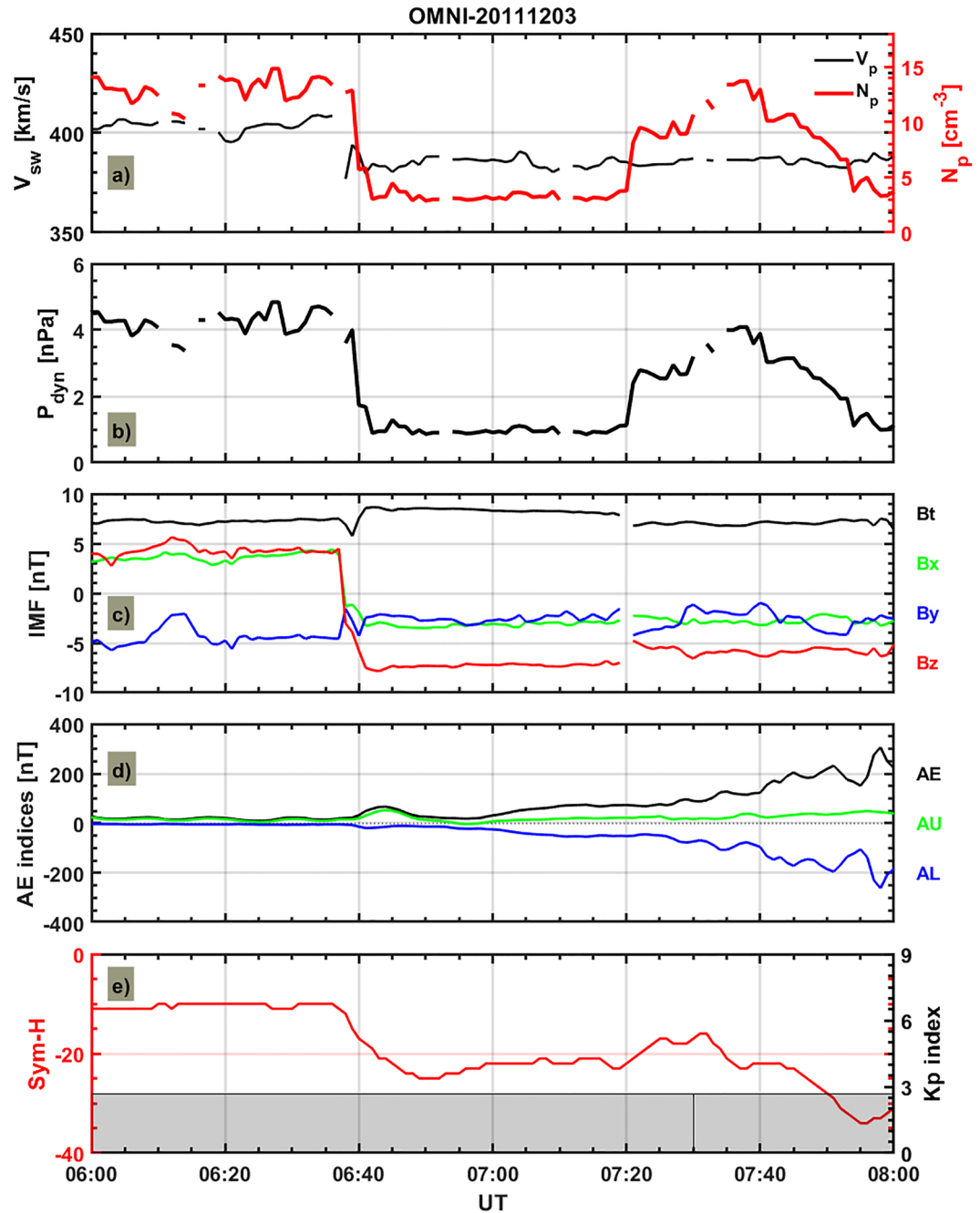


Figure 1. An overview of the solar wind, IMF, AE, Sym-H, and Kp indices from 6:00 to 8:00 UT on 3 December 2011. (a) The solar wind velocity (V_{sw} , black) and proton density (N_p , red); (b) the solar wind dynamic pressure; (c) the IMF strength (B_t , black), B_x (blue), and B_z (red) components; (d) AU (green), AL (blue), and AE (black) indices; (e) the Sym-H (red) and Kp (black shaded) indices. IMF = Interplanetary Magnetic Field.

3. Results

The event was observed on 3 December 2011 during the EISCAT campaign for the Norwegian sounding ICI-3 rocket (Jin et al., 2017, 2019; Spicher et al., 2016). Figures 1a–1c present the upstream solar wind and IMF information from the OMNI data set. The solar wind density (Figure 1a) decreased abruptly from 13 cm^{-3} at 6:39 UT to 3 cm^{-3} at 6:42 UT. This resulted in a sharp decrease in the solar wind dynamic pressure (P_{dyn}) from 4.9 nPa to slightly below 1 nPa (Figure 1b). The IMF was characterized by a sharp southward turn from 6:37 UT to 6:41 UT. The IMF B_y remained negative with decreasing magnitude. The AU, AL and AE indices are shown in Figure 1d.

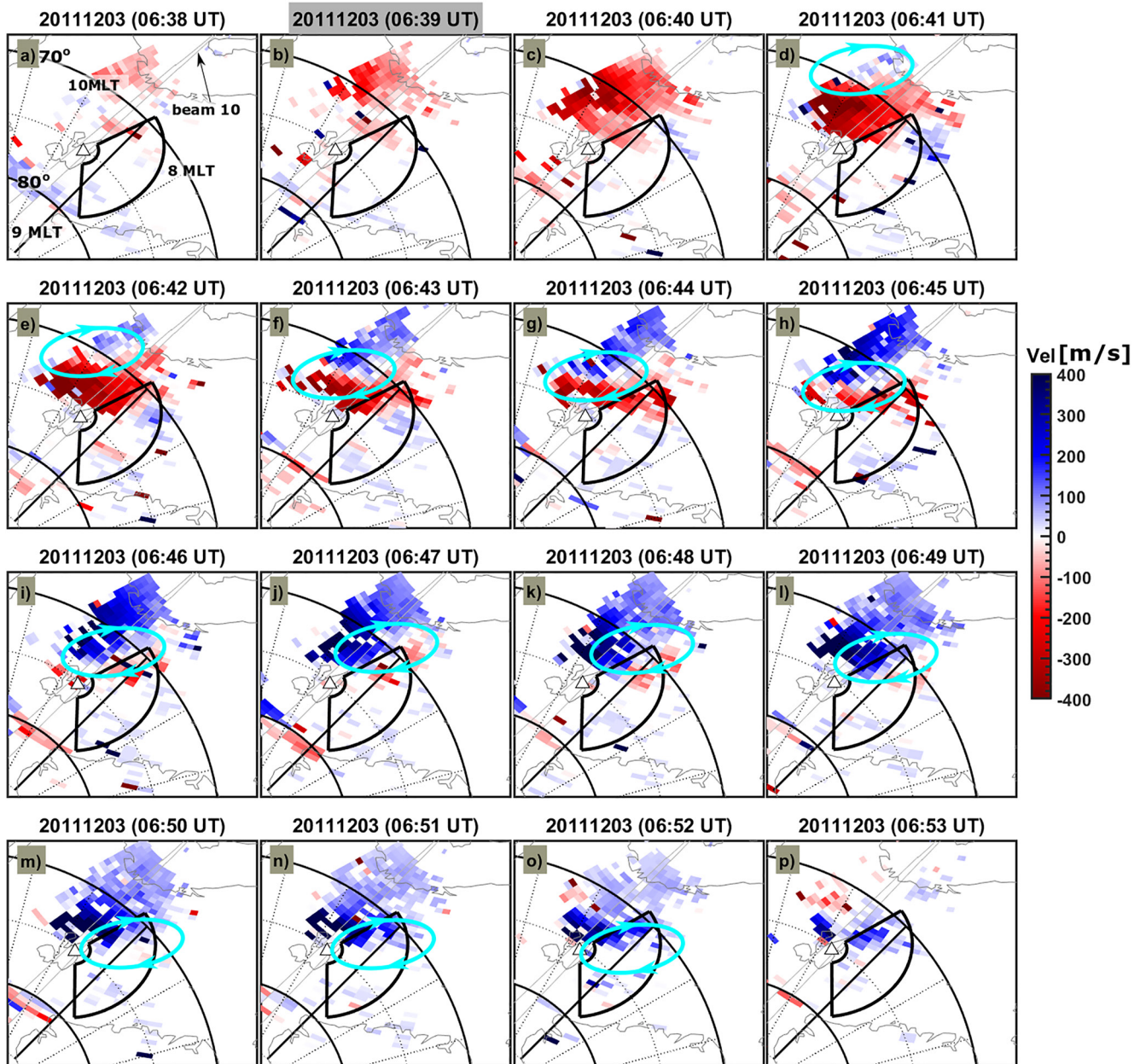


Figure 2. The Doppler drift velocity observed in the field-of-view of the Hankasalmi HF radar with the time cadence of 1 min. The data is presented in magnetic latitude/MLT coordinates, with magnetic noon to the top and dawn to the right. In each panel, the radar beam 10 is marked. The black fan-shaped area is the field-of-view of the European Incoherent Scatter (EISCAT) Svalbard Radar (ESR) 32 m antenna. The white triangle is the location of ESR in Longyearbyen. The enhanced poleward ionospheric flow was first visible at 06:39 UT.

The AL index was relatively stable, while AE and AU slightly increased from ~6:39 UT. The Kp index was stable at 2+, while the Sym-H index decreased quickly from 6:39 UT. The decrease of the Sym-H index was a response of the decrease of solar wind dynamic pressure and a decrease of the magnetopause current (Takeuchi et al., 2002b). We therefore consider 6:39 UT as the time when the solar wind pressure decrease arrived at the dayside magnetosphere.

Figure 2 shows the Doppler drift velocity in the field-of-view (FOV) of the Hankasalmi HF radar. The radar FOV was located in the morning sector (8–10 MLT). The enhanced poleward (red) ionospheric flow was first observed on the eastern side of the FOV around 68° MLAT and 10 MLT (Figure 2b). Then the enhanced flow moved poleward and tailward toward earlier MLT. The first equatorward directed flow was observed at 6:41 UT (Figure 2d).

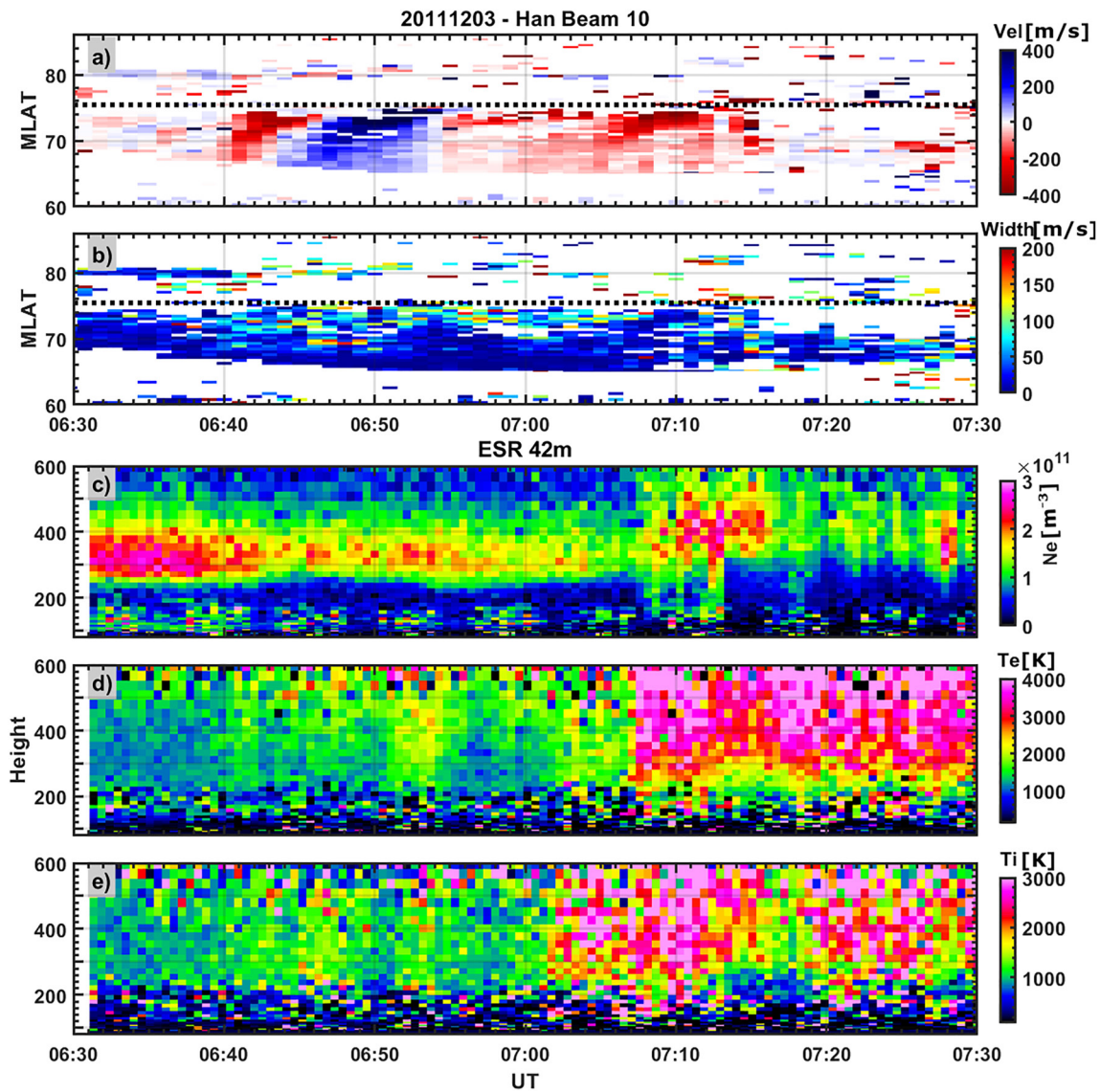


Figure 3. Ionospheric data from the Hankasalmi HF radar and the EISCAT 42 m antenna. The Doppler drift velocity (a) and spectral width (b) from beam 10 of the Hankasalmi HF radar as a function of magnetic latitude (MLAT). The black horizontal dashed line shows the location of the ESR 42 m radar at 75.43° MLAT. The altitude profiles of electron density (c), electron temperature (d), ion temperature (e) from the field-aligned 42 m antenna.

This was a clockwise flow vortex as annotated by the arrowed cyan ellipse. The whole vortex flow moved westward and entered the FOV of the scan mode of the ESR 32 m antenna as indicated by the black fan-shaped area on the westside of Svalbard. The data from ESR 42 m beam (field-aligned in the F region, azimuth 182.1°, elevation 81.6°) is also available. The ESR radar site is annotated by a white triangle in each panel of Figure 2.

The radar beam 10 of the Hankasalmi radar is aligned with ESR (Figure 2a). The range-time plot of data from beam 10 is presented in Figures 3a and 3b, where the black dashed horizontal line shows the location of the ESR site. Figure 3a shows that the poleward directed ionospheric flow reached ESR around 6:45 UT, while the equatorward directed flow reached the ESR site around 6:52 UT. Note that there is a lack of HF backscatter around the ESR site, which could be due to not optimal propagation ray-path of the radar signal. Figure 3b shows the spectral width from beam 10, which shows that the flow vortex was associated with slightly enhanced spectral width. We present the ionospheric data from the ESR 42 m radar in Figures 3c–3e. The electron density profile shows a region of moderate high electron density ($2.5 \times 10^{11} \text{ m}^{-3}$) at ~250–400 km between 6:30–6:40 UT. When the flow vortex reached near the ESR site, the electron density significantly decreased to around $1.5 \times 10^{11} \text{ m}^{-3}$. Interestingly, there was a region of slightly increase (from $1.5 \times 10^{11} \text{ m}^{-3}$ to $2.3 \times 10^{11} \text{ m}^{-3}$ at ~320 km) in

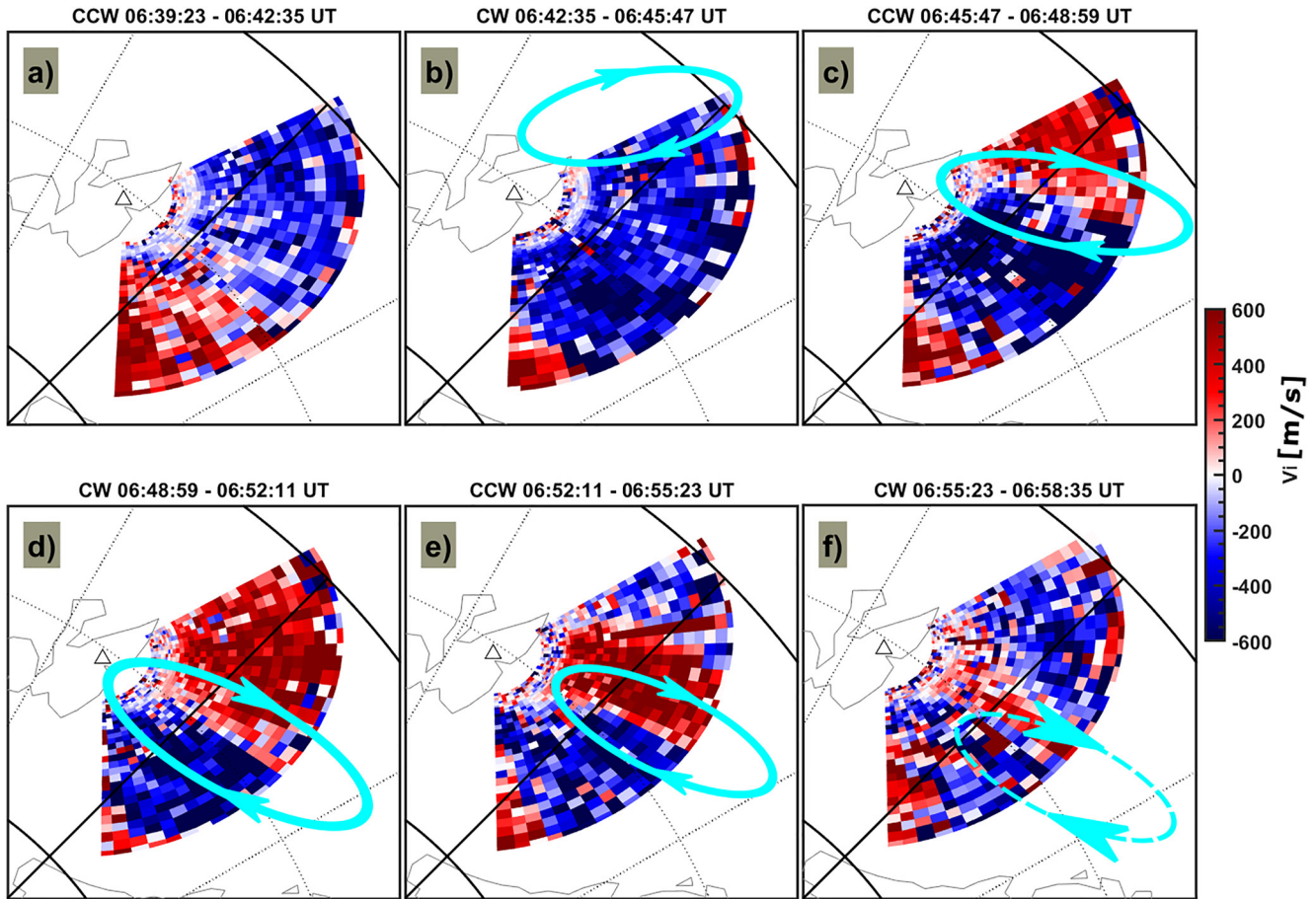


Figure 4. Line-of-sight ion velocity (V_i) observed by the ESR 32 m antenna. Positive (red) velocities are away from the radar site. The scan time is shown on the top of each panel, where “cw” is clockwise and “ccw” is counterclockwise scan. The arrowed cyan ellipse indicates the flow vortex.

electron density around 6:51–6:53 UT. This was at the same time when the equatorward directed flow (blue) reached the ESR site (Figure 3a). The minor increase of the electron density was also associated with the slight increase in the electron temperature. As will be discussed later, this was likely associated with an auroral arc in connection to the flow vortex (Lühr et al., 1996). We also observed weak but identifiable ion temperature associated with the flow vortex. This was likely due to the impact of enhanced ion frictional heating during enhanced ionospheric flow. We note that the ESR 42 m antenna was equatorward of the main auroral oval when the flow vortex was observed (cf. Figure 5). As the IMF B_z turned southward, the main auroral oval expanded equatorward. The main auroral oval should arrive at the ESR site at about 7:07 UT as indicated by the abrupt increase in the electron temperature (Figure 3d). The ongoing soft precipitation also caused enhanced electron density and ion temperature.

The ESR 32 m radar was operating in a fast azimuthal scan mode at an elevation of 30° during this event. Figure 4 shows the ion velocity in 6 azimuthal scans, which show the evolution of the flow vortex when it entered and left the FOV of ESR. Figure 4a shows the scan before the flow vortex entered the FOV of ESR. Figure 4b shows that the poleward directed flow first entered the southern part of the ESR FOV as indicated by the toward (blue) ion velocity. The inferred flow vortex is overlaid as an arrowed cyan ellipse in each panel. The equatorward directed flow entered the FOV in Figure 4c as indicated by away (red) ion velocity from the ESR 32 m radar. The vortex flow continued moving westward and it was barely visible during the scan time in Figure 4f. The flow shear between the positive and negative ion velocity was evidently visible in Figures 4c–4e.

It is also possible to obtain other plasma parameters from the scan mode of the ESR 32 m antenna. Figure 5 shows the ionospheric parameters from the ESR 32 m antenna, which were averaged over altitudes 250–300 km. The data were scanned along fixed range gates and are presented as a function of MLAT. As one azimuthal scan

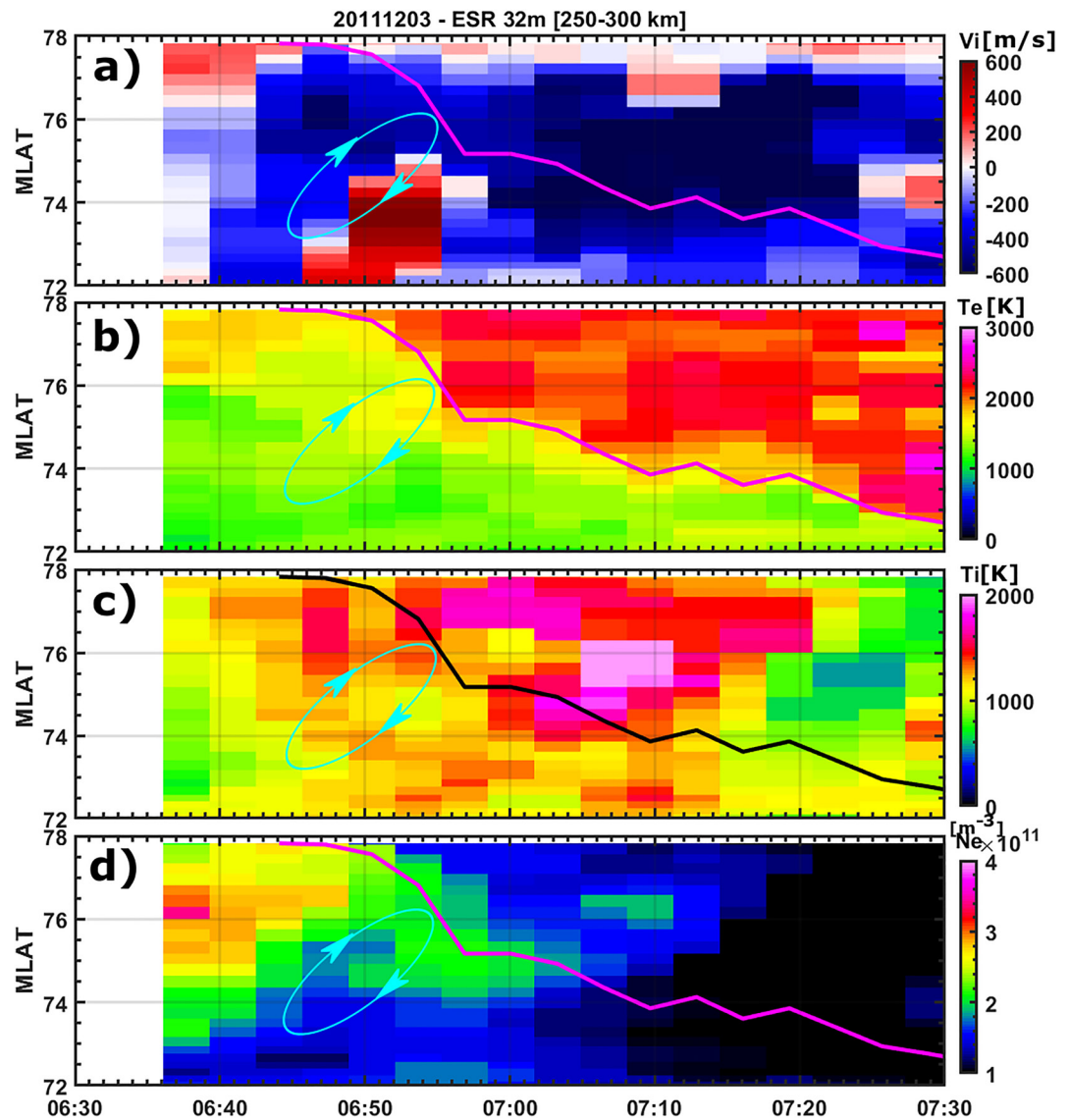


Figure 5. The ionospheric parameters obtained from the ESR 32 m antenna by averaging the data from altitudes between 250–300 km. Line-of-sight ion velocity (a), electron temperature (b), ion temperature (c), and electron density (d). In each panel, the magenta (black in panel c) line marks the equatorward auroral boundary as derived from the electron temperature data by selecting the equatorward boundary at $T_e = 1,800$ K. The arrowed cyan ellipse indicates the flow vortex.

takes 192 s, the time resolution is 192 s in the horizontal axis. The flow vortex can be seen from the ion velocity from blue (toward) near 6:42 UT and red (away) near 6:50 UT. The flow vortex is annotated by the arrowed cyan ellipse in Figure 5. Note that the measured ion velocity is the line-of-sight velocity along the radar beam, that is, it was mainly in the north-south direction below about 74° MLAT, and it became more aligned in the east-west direction above 74° MLAT (cf. Figure 4). Figure 5b shows the electron temperature data. The latitudinal profile of electron temperature can be used to identify the auroral boundary (Doe et al., 2001). The equatorward auroral boundary was obtained by selecting the most equatorward electron temperature that exceeded 1800 K. The derived auroral boundary is plotted as a magenta line in Figures 5a and 5b. The auroral boundary shifted equatorward as a response to the southward turning of the IMF Bz. The equatorward auroral boundary reached 74.3° MLAT (ESR site) at around 7:07 UT. This was consistent with the sudden increase of the electron temperature as measured by the ESR 42 m antenna around the same time (Figure 3d). This justifies that the derived equatorward auroral boundary from the electron temperature data is valid. Notice that the flow vortex was equatorward of the equatorward auroral boundary when it was observed in the FOV of the ESR 32 m antenna. Figure 5c displays the

ion temperature, which shows moderate enhanced T_i in association with the flow vortex. However, the strongest ion temperature enhancement occurred in the auroral zone when there was a strong eastward flow near 75° MLAT around 7:10 UT. The averaged electron density between 250 and 300 km in Figure 5d shows a gradual decrease of electron density that was similar to the ESR 42 m data. Interesting, there was a weak increase of the electron density when the flow vortex was observed, and this coincided with a slight increase of the electron temperature (cf. Figure 4b).

4. Summary and Discussion

In this study, we have presented an event of ionospheric flow vortex that was triggered by a sudden decrease of the solar wind dynamic pressure. The flow vortex was observed in the morning sector ($8\text{--}10$ MLT and $65^\circ\text{--}75^\circ$ MLAT). The 2-D morphology of the flow vortex was clearly observed by both the Hankasalmi coherent scatter HF radar and the azimuthal scan mode of the ESR 32 m radar. The flow vortex was first seen in the eastern FOV of the HF radar, and then it propagated poleward and westward into the FOV of the ESR. When the flow vortex arrived near the ESR site, a gradual decrease of the electron density was observed by the field-aligned 42 m radar. When the equatorward directed ionospheric flow reached the ESR site, weak and visible increases in the electron density and electron temperature were observed. This impact was likely caused by soft electron precipitation associated with the flow vortex (Doe et al., 2001; Lühr et al., 1996). The azimuthal scan mode of the ESR 32 m radar at low elevation angle (30°) allowed us to measure key ionospheric parameters over a larger area (6° in MLAT and 120° in azimuthal angle). Velocity shear associated with the flow vortex was clearly visible in 3 scans (3×192 s = 9.6 min). The latitudinal scan of the electron temperature at 250–300 km was obtained in order to proxy the equatorward auroral boundary. Apparently, the flow vortex was located in the subauroral region in the morning sector (cf. Figure 5). This is consistent with the studies of magnetic signature of TCVs, that is, the TCV center is located in the closed field line within the region of plasmasheet (Moretto & Yahnin, 1998).

In the dayside polar ionosphere, the impact of soft particle precipitation and the solar EUV radiation can be easily distinguished from each other. For example, soft particle precipitation can be easily seen from pulsed electron temperature enhancements near the dayside cusp region. This is a distinctive feature from the electron heating by the sunlight, which is a smooth increase of electron temperature with increasing solar elevation angle. We also note that during this day, the ESR was in the darkness. See also Figure 7 of Lorentzen et al. (2010) during a similar day of year (8 December 2008), which shows that ESR was in the darkness. The solar photons were not expected to affect the electron temperature around 07 UT for our event. This suggests that the electron temperature can be used to proxy the OCB around the cusp ionosphere. According to the Newell's model (Newell et al., 2007), the OCB location should be around 78° MLAT for $d\Phi/dt = 1,000$ at around 6:37 UT. This is very consistent with the proxy of OCB obtained from enhanced T_e . As it often happens, the sudden decrease of the solar wind dynamic pressure occurred in association with the orientation change of the IMF, that is, the sudden decrease in the solar wind dynamics pressure was associated with a southward turning of the IMF Bz. However, we can rule out the contribution of the southward turning of the IMF due to two reasons: (a) the flow vortex occurred equatorward of the auroral boundary, and it originated at lower latitudes and moved poleward and westward; while the FTE induced flow occurs near the open/closed field line boundary and propagates poleward; (b) the FTE driven flow is poleward during negative Bz (Cowley & Lockwood, 1992; Southwood, 1987), and this contradicts with the equatorward directed flow in the flow vortex. Note that this is also different from the reversed flow event (RFE) in the cusp ionosphere (Jin et al., 2019; Moen et al., 2008; Rinne et al., 2007). The RFE is interpreted as the return flow on the poleward side of the newly reconnected flux tube in the cusp region (see Figure 7 in Jin et al., 2019). On the contrary, the equatorward return flow of the flow vortex occurred on the equatorward side in our event. In addition, the reversed flow event occurs on the open field line region, while the present event occurred in closed field line. Actually, a series of reversed flow events were indeed observed in the cusp ionosphere later this day (see e.g., Jin et al., 2019), but they were not related to the event in this study.

There are a few studies that focused on the impact on the ionospheric response to SI+ and TCV. For example, Kataoka et al. (2003) observed transient production of F-region irregularities during the passage of TCV. Valladares et al. (1999) observed electron density depletion by a factor of two associated with a TCV event. The decreased electron density was explained by the fast ionospheric flow and ion frictional heating with subsequent increased recombination rate. In our event, we also observed a decrease of electron density (from $2.5 \times 10^{11} \text{ m}^{-3}$ to $1.5 \times 10^{11} \text{ m}^{-3}$) during the passage of the flow vortex. The ion temperature was also enhanced. This indicates that

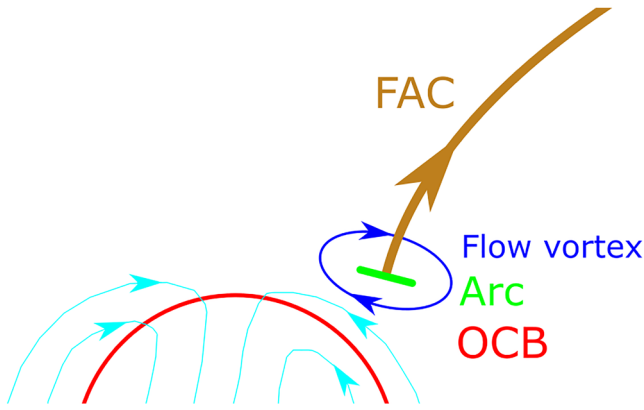


Figure 6. Schematics of the observation scenario. The observed clockwise ionospheric flow vortex is equatorward of the main auroral oval, and it is associated with an upward field aligned current (FAC) and downward electron precipitation. OCB = open/closed field line boundary.

the decrease of electron density should be related to fast flows, as suggested by Valladares et al. (1999) and Ogawa et al. (2001).

Unlike the impact of solar wind dynamic pressure increases, the impact of solar wind dynamic pressure decreases are relatively less studied in the literature. Zhao et al. (2016) observed magnetospheric flow vortex driven by a negative solar wind dynamic pressure pulse, where the observed vortex rotated in a direction opposite to the case due to positive solar wind dynamic pressure pulses. The negative solar wind pressure can induce FACs in the dawn and dusk sectors by Region 2 sense FACs, that is, it flows out of (into) the ionosphere in the dawnside (duskside) (Zhao et al., 2016).

Based on the previous literature and our observations, we summarize the observation scenario in Figure 6. The clockwise ionospheric flow vortex was observed in the morning side ionosphere and it was equatorward of the main auroral oval. Due to the fast flow (or flow shear) associated with the flow vortex, the electron density was significantly depleted within 10 min. The clockwise flow vortex was connected to the magnetosphere through an upward FAC, which was associated with an auroral arc due to accelerated electron precipitation. The soft precipitation caused weak enhancement of ionospheric density and electron temperature. Note that in our interpretation

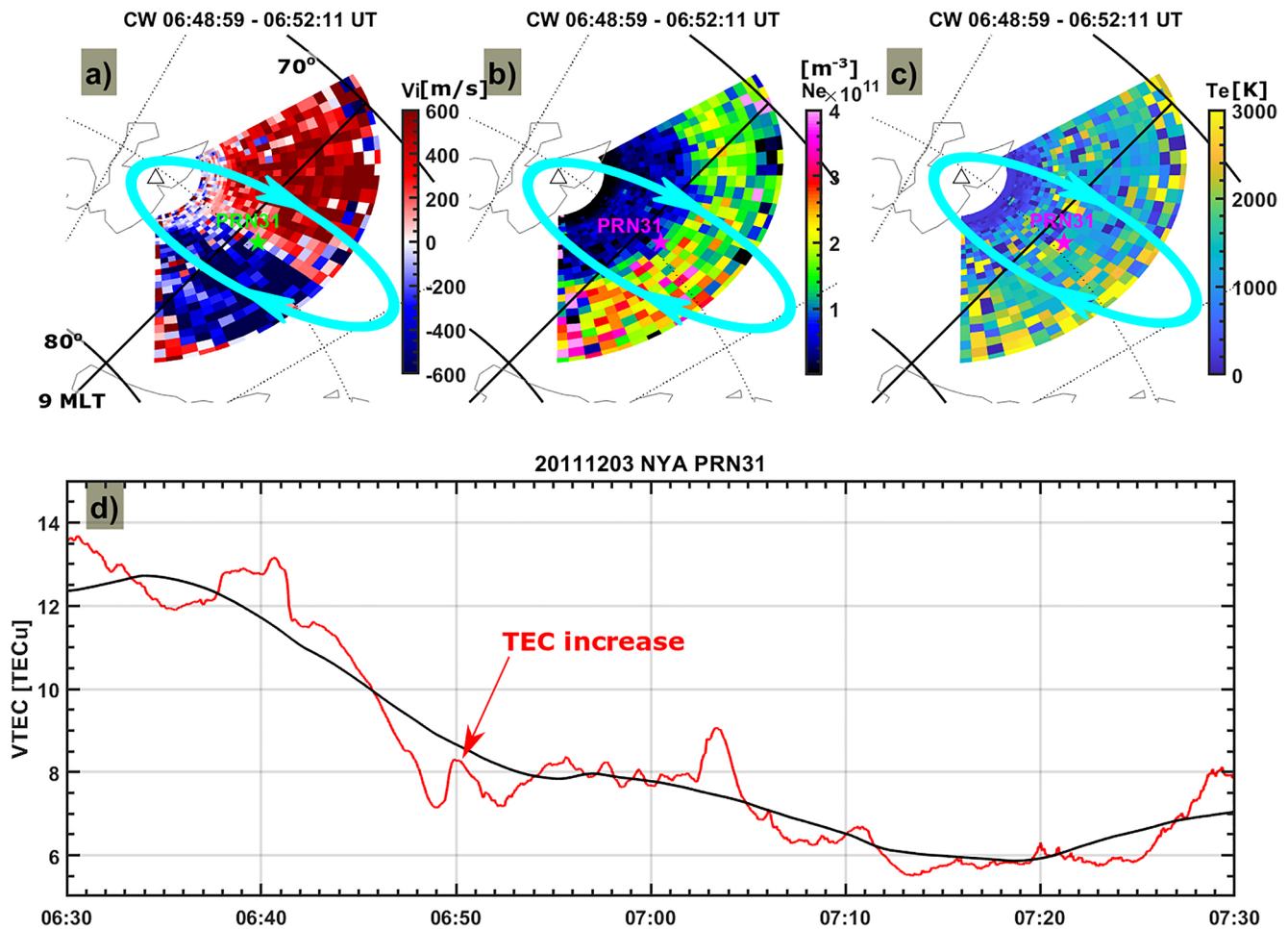


Figure 7. The observations from the ESR 32 m antenna and the vertical GPS TEC data from Ny-Ålesund (NYA). The line-of-sight ion velocity (a), electron density (b), and the electron temperature (c) from the scan of the ESR 32 m antenna. The pierce point of PRN31 at an altitude of 300 km is plotted as an asterisk in each panel. (d) The 1-Hz resolution VTEC (red) and its moving average (black) from PRN31 tracked in Ny-Ålesund.

(Figure 6), the auroral arc is detached from the dayside auroral zone (OCB). This is similar to the observations by Lühr et al. (1996). However, Kim et al. (2017) presented a “throat” aurora-like event during the passage of a TCV event (where the aurora associated with TCV is connected to the cusp auroral region). The existence of throat aurora is not contradictory to our explanation. In the “classical” view, the dayside OCB is smooth roughly at constant MLAT. However, Han et al. (2019) showed that the dayside OCB can be quite irregular by using 2-D auroral images instead of the traditional keogram or Meridian Scanning Photometer in the 1-D sense. Unfortunately, we do not have ground-based optics (due to the cloud coverage) to indicate the linkage of flow vortex to throat aurora (Kim et al., 2017) or discrete auroral arc equatorward of cusp as in Lühr et al. (1996). Therefore, we still utilize the classical view of smooth OCB and magnetopause boundary (similar to Lühr et al. (1996) and Glassmeier et al. (1989)) and show that the flow vortex is equatorward of the classical OCB. It remains an open question whether the auroral arc associated with the clockwise flow is a detached arc or the aurora is connected to the cusp auroral region (i.e., throat aurora). Further studies are needed to give a detailed description of the connectivity of the FAC related auroral arc with respect to the cusp aurora.

We note that our observations are in the morning sector. The scenario should be opposite in the dusk sector. For example, Liu et al. (2011) presented an event of decreased auroral intensity in response to an interplanetary shock in the afternoon sector from Zhongshan Station in the Antarctic. This is explained by the downward FAC in the afternoon sector at the beginning of the sudden commencement. Zhao et al. (2019) showed observational evidence for enhancement in auroral intensity caused by FACs under solar wind dynamic pressure decrease. Shi et al. (2020) proposed that the auroral intensity can be increased or decreased in different regions for upward or downward FACs caused by solar wind dynamic pressure increase and decrease. A model is summarized and presented in Shi et al. (2020). Later on, Zhao et al. (2021) showed observational evidence for different variations in auroral intensity caused by FACs under solar wind dynamic pressure increase. Note that the illustration of the global response to sudden changes in the solar wind dynamic pressure proposed by Shi et al. (2020) was mainly based on observations in the magnetosphere. Therefore, this present study of the responses of the ionospheric vortex caused by sudden pressure decrease represents an important support for the global picture of the magnetosphere-ionosphere system. Given the observational feature in the ionosphere, this phenomenon should also be detectable by using ground-based GPS TEC data. For example, Jin et al. (2016) presented an event showing the global TEC response of the auroral ionosphere due to the sudden increase of the solar wind dynamic pressure associated with an interplanetary shock. The fast anti-sunward propagation of TEC enhancements due to shock-induced aurora was observed. Similarly, we show that it is also possible to detect the TEC response due to the solar wind pressure decrease by coordinated observations. Figures 7a–7c show the ion velocity, electron density and electron temperature during the azimuthal scan at 6:48:59–6:52:11 UT. The ionospheric parameters during other azimuthal scan times can be found in the Supporting Information S1 (Figures S1–S3). The pierce point of PRN31 tracked from Ny-Ålesund is shown as an asterisk, which was located near the flow shear during this scan. The pierce point is projected to an altitude of 300 km according to the electron density profile in Figure 3c. Figures 7b and 7c show moderate electron density as well as noisy and enhanced electron temperature. The minor increase in the electron density and temperature can be also seen from Figures 3c and 3d as well as Figures 5b and 5d. However, due to the noisiness of the ESR data, it is difficult to conclude whether the electron density and temperature indeed increased near the flow shear. Figure 7d shows the 1-Hz resolution GPS TEC data from PRN31 (red) and its moving average (black) in a sliding window of 15 min. Clearly, the TEC data shows gradual decrease from 6:40 UT onward. There was a minor increase in the TEC data from 6:48:30 UT to 6:52 UT. This was the time when PRN31 was located near the flow shear during the scan in Figures 7a–7c. The minor TEC increase ($\Delta\text{TEC} \approx 1 \text{ TECu}$, where $1 \text{ TECu} = 10^{16} \text{ electrons/m}^2$) was likely caused by the auroral particle precipitation near the flow shear. This confirms that the weak increases in electron density and electron temperature by the ESR should be real. This also demonstrates that it is possible to detect the ionospheric effect due to sudden solar wind dynamic pressure decrease by using the GPS TEC data. By using the global distributed networks of GPS receivers (Jin et al., 2016), one can investigate the propagation and evolution of the associated ionospheric effect. This provides another alternative data set (in addition to magnetometers and optical auroral data) to study the response and evolution of the magnetosphere-ionosphere system due to the impact of the negative solar wind pressure pulse. Such studies will be explored in future investigations.

Data Availability Statement

The IMF and solar wind data are provided by the NASA OMNIWeb service (<http://omniweb.gsfc.nasa.gov>). EISCAT is an international association supported by research organizations in China (CRIRP), Finland (SA), Japan (NIPR and STEL), Norway (NFR), Sweden (VR), and the United Kingdom (NERC). Data from EISCAT can be obtained from the Madrigal database <https://eiscat.se/>. SuperDARN is a collection of radars funded by national scientific funding agencies of Australia, Canada, China, France, Japan, South Africa, United Kingdom, and the United States of America. The SuperDARN data can be obtained from <http://vt.superdarn.org/tiki-index.php>. The GPS data can be obtained through <https://cddis.nasa.gov/archive/gnss/data/highrate/>.

Acknowledgments

YJ and WJM acknowledge funding from the European Research Council (ERC) under the European Union's Horizon 2020 research and innovation programme (ERC Consolidator Grant 866357, POLAR-4DSpace). This research is a part of the 4DSpace Strategic Research Initiative at the University of Oslo. AS acknowledges funding from the RCN Grant 326039, and the UiT The Arctic University of Norway contribution to the EISCAT 3D (RCN funded Grant 245683). JL acknowledges funding from the National Scientific Foundation of China (Grants 42120104003 and 42374208).

References

- Araki, T. (1994). A physical model of the geomagnetic sudden commencement. In *Solar wind sources of magnetospheric ultra-low-frequency waves* (pp. 183–200). <https://doi.org/10.1029/GM081p0183>
- Araki, T., & Nagano, H. (1988). Geomagnetic response to sudden expansions of the magnetosphere. *Journal of Geophysical Research*, 93(A5), 3983–3988. <https://doi.org/10.1029/JA093iA05p03983>
- Carlson, H. C., Oksavik, K., Moen, J., van Eyken, A. P., & Guio, P. (2002). ESR mapping of polar-cap patches in the dark cusp. *Geophysical Research Letters*, 29(10), 241–244. <https://doi.org/10.1029/2001gl014087>
- Collis, P. N., & Haggstrom, I. (1991). High-latitude ionospheric response to a geomagnetic sudden commencement. *Journal of Atmospheric and Terrestrial Physics*, 53(3–4), 241–248. [https://doi.org/10.1016/0021-9169\(91\)90108-j](https://doi.org/10.1016/0021-9169(91)90108-j)
- Cowley, S. W. H., & Lockwood, M. (1992). Excitation and decay of solar wind-driven flows in the magnetosphere-ionosphere system. *Annales Geophysicae-Atmospheres Hydrospheres and Space Sciences*, 10(1–2), 103–115. Retrieved from <Go to ISI>://WOS:A1992HL02700010
- Doe, R. A., Kelly, J. D., & Sanchez, E. R. (2001). Observations of persistent dayside F region electron temperature enhancements associated with soft magnetosheathlike precipitation. *Journal of Geophysical Research*, 106(A3), 3615–3630. <https://doi.org/10.1029/2000ja000186>
- Dungey, J. W. (1961). Interplanetary magnetic field and auroral zones. *Physical Review Letters*, 6(2), 47–48. <https://doi.org/10.1103/PhysRevLett.6.47>
- Friis-Christensen, E., McHenry, M., Clauer, C., & Vennerstrøm, S. (1988). Ionospheric traveling convection vortices observed near the polar cleft: A triggered response to sudden changes in the solar wind. *Geophysical Research Letters*, 15(3), 253–256. <https://doi.org/10.1029/GL015i003p00253>
- Glassmeier, K.-H., Hönisch, M., & Untiedt, J. (1989). Ground-based and satellite observations of traveling magnetospheric convection twin vortices. *Journal of Geophysical Research*, 94(A3), 2520–2528. <https://doi.org/10.1029/JA094iA03p02520>
- Greenwald, R. A., Baker, K. B., Dudeney, J. R., Pinnock, M., Jones, T. B., Thomas, E. C., et al. (1995). Darn superdarn—A global view of the dynamics of high-latitude convection. *Space Science Reviews*, 71(1–4), 761–796. <https://doi.org/10.1007/Bf00751350>
- Haerendel, G., Paschmann, G., Sckopke, N., Rosenbauer, H., & Hedgecock, P. C. (1978). Frontside boundary-layer of magnetosphere and problem of reconnection. *Journal of Geophysical Research*, 83(NA7), 3195–3216. <https://doi.org/10.1029/JA083iA07p03195>
- Han, D.-S., Xu, T., Jin, Y., Oksavik, K., Chen, X.-C., Liu, J.-J., et al. (2019). Observational evidence for throat aurora being associated with magnetopause reconnection. *Geophysical Research Letters*, 46(13), 7113–7120. <https://doi.org/10.1029/2019GL083593>
- Hori, T., Shinbori, A., Nishitani, N., Kikuchi, T., Fujita, S., Nagatsuma, T., et al. (2012). Evolution of negative SI-induced ionospheric flows observed by SuperDARN King Salmon HF radar. *Journal of Geophysical Research*, 117(A12), A12223. <https://doi.org/10.1029/2012ja018093>
- Jin, Y., Moen, J. I., Spicher, A., Oksavik, K., Miloch, W. J., Clausen, L. B. N., et al. (2019). Simultaneous rocket and scintillation observations of plasma irregularities associated with a reversed flow event in the cusp ionosphere. *Journal of Geophysical Research: Space Physics*, 124(8), 7098–7111. <https://doi.org/10.1029/2019ja026942>
- Jin, Y. Q., Moen, J. I., Oksavik, K., Spicher, A., Clausen, L. B. N., & Miloch, W. J. (2017). GPS scintillations associated with cusp dynamics and polar cap patches. *Journal of Space Weather and Space Climate*, 7, A23. <https://doi.org/10.1051/swsc/2017022>
- Jin, Y. Q., Zhou, X. Y., Moen, J. I., & Hairston, M. (2016). The auroral ionosphere TEC response to an interplanetary shock. *Geophysical Research Letters*, 43(5), 1810–1818. <https://doi.org/10.1002/2016gl067766>
- Kataoka, R., Fukunishi, H., Hosokawa, K., Fujiwara, H., Yukimatu, A. S., Sato, N., & Tung, Y. K. (2003). Transient production of F-region irregularities associated with TCV passage. *Annales Geophysicae*, 21(7), 1531–1541. <https://doi.org/10.5194/angeo-21-1531-2003>
- Kim, H., Lessard, M. R., Jones, S. L., Lynch, K. A., Fernandes, P. A., Aruliah, A. L., et al. (2017). Simultaneous observations of traveling convection vortices: Ionosphere-thermosphere coupling. *Journal of Geophysical Research: Space Physics*, 122(5), 4943–4959. <https://doi.org/10.1002/2017ja023904>
- King, J. H., & Papitashvili, N. E. (2005). Solar wind spatial scales in and comparisons of hourly Wind and ACE plasma and magnetic field data. *Journal of Geophysical Research*, 110(A2), A02104. <https://doi.org/10.1029/2004ja010649>
- Liu, J., Chakraborty, S., Chen, X., Wang, Z., He, F., Hu, Z., et al. (2023). Transient response of polar-cusp ionosphere to an interplanetary shock. *Journal of Geophysical Research: Space Physics*, 128(3), e2022JA030565. <https://doi.org/10.1029/2022JA030565>
- Liu, J., Hu, H., Han, D., Yang, H., & Lester, M. (2015). Simultaneous ground-based optical and SuperDARN observations of the shock aurora at MLT noon. *Earth Planets and Space*, 67(1), 120. <https://doi.org/10.1186/s40623-015-0291-2>
- Liu, J. J., Hu, H. Q., Han, D. S., Araki, T., Hu, Z. J., Zhang, Q. H., et al. (2011). Decrease of auroral intensity associated with reversal of plasma convection in response to an interplanetary shock as observed over Zhongshan station in Antarctica. *Journal of Geophysical Research*, 116(A3), A03210. <https://doi.org/10.1029/2010JA016156>
- Lockwood, M., & Hapgood, M. A. (1998). On the cause of a magnetospheric flux transfer event. *Journal of Geophysical Research*, 103(A11), 26453–26478. <https://doi.org/10.1029/98ja02244>
- Lorentzen, D. A., Moen, J., Oksavik, K., Sigernes, F., Saito, Y., & Johnsen, M. G. (2010). In situ measurement of a newly created polar cap patch. *Journal of Geophysical Research*, 115(A12), A12323. <https://doi.org/10.1029/2010JA015710>
- Lühr, H., Lockwood, M., Sandholt, P. E., Hansen, T. L., & Moretto, T. (1996). Multi-instrument ground-based observations of a travelling convection vortices event. *Annales Geophysicae-Atmospheres Hydrospheres and Space Sciences*, 14(2), 162–181. <https://doi.org/10.1007/s00585-996-0162-z>
- Lyatsky, W. B., Sofko, G. J., Kustov, A. V., Andre, D., Hughes, W. J., & Murr, D. (1999). Traveling convection vortices as seen by the SuperDARN HF radars. *Journal of Geophysical Research*, 104(A2), 2591–2601. <https://doi.org/10.1029/1998ja000007>

- Meurant, M., Gérard, J.-C., Hubert, B., Coumans, V., Blockx, C., Østgaard, N., & Mende, S. B. (2003). Dynamics of global scale electron and proton precipitation induced by a solar wind pressure pulse. *Geophysical Research Letters*, *30*(20), 2032. <https://doi.org/10.1029/2003GL018017>
- Milan, S. E., Davies, J. A., & Lester, M. (1999). Coherent HF radar backscatter characteristics associated with auroral forms identified by incoherent radar techniques: A comparison of CUTLASS and EISCAT observations. *Journal of Geophysical Research*, *104*(A10), 22591–22604. <https://doi.org/10.1029/1999ja900277>
- Moen, J., Rinne, Y., Carlson, H. C., Oksavik, K., Fujii, R., & Opgenoorth, H. (2008). On the relationship between thin Birkeland current arcs and reversed flow channels in the winter cusp/cleft ionosphere. *Journal of Geophysical Research*, *113*(A9), A09220. <https://doi.org/10.1029/2008ja013061>
- Moretto, T., & Yahnin, A. (1998). Mapping travelling convection vortex events with respect to energetic particle boundaries. *Annales Geophysicae*, *16*(8), 891–899. <https://doi.org/10.1007/s00585-998-0891-2>
- Newell, P. T., Sotirelis, T., Liou, K., Meng, C. I., & Rich, F. J. (2007). A nearly universal solar wind-magnetosphere coupling function inferred from 10 magnetospheric state variables. *Journal of Geophysical Research*, *112*(A1), A01206. <https://doi.org/10.1029/2006ja012015>
- Ogawa, T., Buchert, S. C., Nishitani, N., Sato, N., & Lester, M. (2001). Plasma density suppression process around the cusp revealed by simultaneous CUTLASS and EISCAT Svalbard radar observations. *Journal of Geophysical Research*, *106*(A4), 5551–5564. <https://doi.org/10.1029/2000ja900111>
- Ribeiro, A. J., Ruohoniemi, J. M., Ponomarenko, P. V., Clausen, L. B. N., Baker, J. B. H., Greenwald, R. A., et al. (2013). A comparison of SuperDARN ACF fitting methods. *Radio Science*, *48*(3), 274–282. <https://doi.org/10.1002/rd.20031>
- Rinne, Y., Moen, J., Oksavik, K., & Carlson, H. C. (2007). Reversed flow events in the winter cusp ionosphere observed by the European Incoherent Scatter (EISCAT) Svalbard radar. *Journal of Geophysical Research*, *112*(A10), A10313. <https://doi.org/10.1029/2007ja012366>
- Russell, C. T., & Elphic, R. C. (1978). Initial ISEE magnetometer results—Magnetopause observations. *Space Science Reviews*, *22*(6), 681–715. <https://doi.org/10.1007/BF00212619>
- Russell, C. T., & Elphic, R. C. (1979). ISEE observations of flux-transfer events at the dayside magnetopause. *Geophysical Research Letters*, *6*(1), 33–36. <https://doi.org/10.1029/GL006i001p00033>
- Schunk, R. W., Zhu, L., & Sojka, J. J. (1994). Ionospheric response to traveling convection twin vortices. *Geophysical Research Letters*, *21*(17), 1759–1762. <https://doi.org/10.1029/94GL01059>
- Shi, Q. Q., Shen, X.-C., Tian, A. M., Degeling, A. W., Zong, Q., Fu, S. Y., et al. (2020). Magnetosphere response to solar wind dynamic pressure change. In *Dayside magnetosphere interactions* (pp. 77–97). <https://doi.org/10.1002/9781119509592.ch5>
- Southwood, D. J. (1987). The ionospheric signature of flux-transfer events. *Journal of Geophysical Research*, *92*(A4), 3207–3213. <https://doi.org/10.1029/JA092iA04p03207>
- Spicher, A., Ilyasov, A. A., Miloch, W. J., Chernyshov, A. A., Clausen, L. B. N., Moen, J. I., et al. (2016). Reverse flow events and small-scale effects in the cusp ionosphere. *Journal of Geophysical Research-Space Physics*, *121*(10), 10466–10480. <https://doi.org/10.1002/2016ja022999>
- Takeuchi, T., Araki, T., Viljanen, A., & Watermann, J. (2002a). Geomagnetic negative sudden impulses: Interplanetary causes and polarization distribution. *Journal of Geophysical Research*, *107*(A7), SMP7-1–SMP7-14. <https://doi.org/10.1029/2001JA900152>
- Takeuchi, T., Araki, T., Viljanen, A., & Watermann, J. (2002b). Geomagnetic negative sudden impulses: Interplanetary causes and polarization distribution. *Journal of Geophysical Research*, *107*(A7), 1096. <https://doi.org/10.1029/2001ja900152>
- Valladares, C. E., Alcaydé, D., Rodriguez, J. V., Ruohoniemi, J. M., & Van Eyken, A. P. (1999). Observations of plasma density structures in association with the passage of traveling convection vortices and the occurrence of large plasma jets. *Annales Geophysicae*, *17*(8), 1020–1039. <https://doi.org/10.1007/s00585-999-1020-6>
- Wannberg, G., Wolf, I., Vanhainen, L. G., Koskenniemi, K., Rottger, J., Postila, M., et al. (1997). The EISCAT svalbard radar: A case study in modern incoherent scatter radar system design. *Radio Science*, *32*(6), 2283–2307. <https://doi.org/10.1029/97rs01803>
- Zhao, H. Y., Shen, X. C., Tang, B. B., Tian, A. M., Shi, Q. Q., Weygand, J. M., et al. (2016). Magnetospheric vortices and their global effect after a solar wind dynamic pressure decrease. *Journal of Geophysical Research-Space Physics*, *121*(2), 1071–1077. <https://doi.org/10.1002/2015ja021646>
- Zhao, H. Y., Zhou, X. Z., Zong, Q. G., Weygand, J. M., Shi, Q. Q., Liu, Y., et al. (2019). Small-scale aurora associated with magnetospheric flow vortices after a solar wind dynamic pressure decrease. *Journal of Geophysical Research-Space Physics*, *124*(5), 3303–3311. <https://doi.org/10.1029/2018ja026234>
- Zhao, J. Y., Shi, Q. Q., Tian, A. M., Shen, X. C., Weygand, J. M., Wang, H. Z., et al. (2021). Vortex generation and auroral response to a solar wind dynamic pressure increase: Event analyses. *Journal of Geophysical Research: Space Physics*, *126*(3), e2020JA028753. <https://doi.org/10.1029/2020ja028753>
- Zhou, X. Y., Strangeway, R. J., Anderson, P. C., Sibeck, D. G., Tsurutani, B. T., Haerendel, G., & Arballo, J. K. (2003). Shock aurora: FAST and DMSP observations. *Journal of Geophysical Research*, *108*(A4), 8019. <https://doi.org/10.1029/2002ja009701>
- Zhou, X. Y., & Tsurutani, B. T. (1999). Rapid intensification and propagation of the dayside aurora: Large scale interplanetary pressure pulses (fast shocks). *Geophysical Research Letters*, *26*(8), 1097–1100. <https://doi.org/10.1029/1999gl900173>
- Zou, S., Ozturk, D., Varney, R., & Reimer, A. (2017). Effects of sudden commencement on the ionosphere: PFISR observations and global MHD simulation. *Geophysical Research Letters*, *44*(7), 3047–3058. <https://doi.org/10.1002/2017GL072678>